Journal of Manufacturing Processes 83 (2022) 203–211

Contents lists available at ScienceDirect

Journal of Manufacturing Processes

journal homepage: www.elsevier.com/locate/manpro

Multi-layer thermo-fluid modeling of powder bed fusion (PBF) process

Behzad Fotovvati *, Kevin Chou

Additive Manufacturing Institute of Science and Technology (AMIST), University of Louisville, Louisville, KY 40292, USA

ARTICLE INFO

Keywords:
Multi-layer simulation
Powder-bed fusion
Selective laser melting
Discrete element method
Computational fluid dynamics

ABSTRACT

In this study, a 3D thermo-fluid computational method has been developed and employed to simulate the laser powder bed fusion (PBF) process. The particular objective is to demonstrate the feasibility of multi-layer simulations of the laser PBF process and to discuss the potential and challenges of this approach. The approach includes using the discrete element method (DEM) to simulate particle spreading on a powder bed, as well as computational fluid dynamics (CFD) and heat transfer to simulate laser-powder/matter interactions, in a sequential manner to about 10 layers only with a small scan area, limited by currently available computational power. The simulation results can offer insight such as melt pool shapes and sizes, also solidified surface morphology along different build layers. The model also includes a surface tracking algorithm to account for the formation of voids and lack-of-fusion pores. In addition to achieving the main objective of this study, i.e., feasibility demonstration of this computational process, it is also noted that, for the case studied, the defects in a former layer may shrink, or even vanish, due to the extra thermal energy received from laser scanning of subsequent layers. This study has successfully demonstrated the sequential linkage between a discrete element method and a thermo-fluid model in a multi-layer deposition fashion and the experimental validation will be performed in future work. With significantly greater computational capabilities in the future, the developed method may potentially be utilized as a means to understand physical phenomena and select key process parameters for PBF fabrications of small features.

1. Introduction

Powder bed fusion (PBF) is an additive manufacturing technique that involves the repeated deposition of powder particles and selective melting of them in a layer-wise manner. This process is categorized into different types based on the applied heat source, which is either a laser beam in selective laser melting (SLM) [1] and selective laser sintering (SLS) [2], or an electron beam in electron beam melting (EBM) [3]. PBF has several advantages, e.g., design freedom, less material waste, etc., over conventional manufacturing methods [4]. The implementation of numerical simulations plays a crucial role in the detailed understanding of the PBF process and the optimization of its parameters. Several influential characteristics of the process, such as powder particle distribution and defect formation, which may be difficult for experimental investigation or too costly with in-situ monitoring techniques [5], are facilitated through numerical simulations, such as the integrated discrete element method (DEM) and computational fluid dynamics (CFD). In other words, numerical simulations can be less expensive alternatives for experiments to study multi-physics phenomena involved in the PBF process, such as evaporation, fluid flow, melting/solidification, recoil pressure, etc.

Various numerical models of the PBF process have been implemented in the literature. They include thermal finite element (FE) models for several purposes, including the prediction of phase transformation and analyzing lack-of-fusion defect formation [6], the observation and prediction of the variations in the melt pool dimensions [7,8], the investigation of the effects of the process parameters on the melt pool dimensions [9–11], and to optimize the scan strategy [12], thermo-metallurgical models to calculate the solidification parameters from the temperature fields and use existing theoretical models to obtain the grain size and morphology of the PBF-fabricated samples [13,14], and thermo-mechanical models to investigate the effects of temperature distribution resulted from different scan strategies and PBF process parameters on the formation of residual stresses [15–19] thus on part deflections [20–23]. By reviewing different types of models presented in the literature, it can be concluded that the best-suited models for multi-layer simulation of the PBF process are thermo-fluid models with surface-tracking capabilities, where the fluid's free surface dynamics

* Corresponding author.
E-mail address: b.fotovvati@louisville.edu (B. Fotovvati).

https://doi.org/10.1016/j.jmapro.2022.09.003
Received 27 May 2022; Received in revised form 1 September 2022; Accepted 3 September 2022

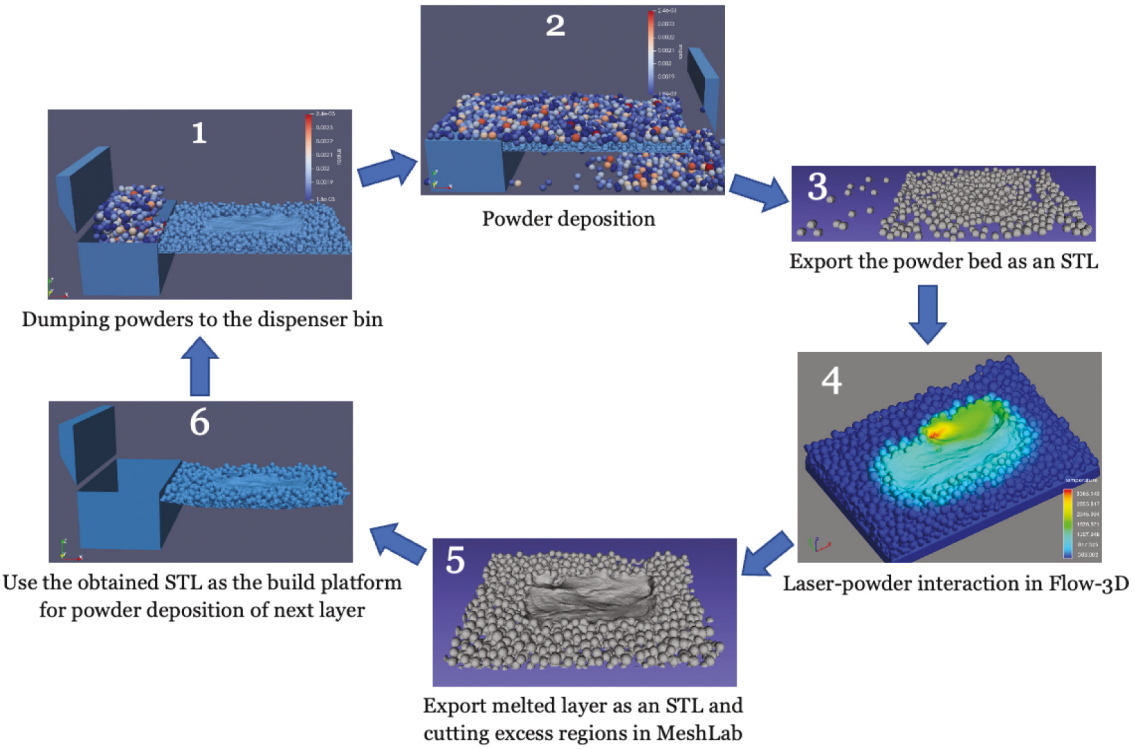

Fig. 1. The multi-layer simulation methodology.

also give the ability to simulate the formation and evolution of porosity between different layers during the process.

Thermo-fluid models are among the best-suited computational techniques for single-layer and multi-layer simulation of the PBF process [24]. By developing a thermo-fluid model of a single scan track in the laser powder bed fusion (L-PBF) process, Wu et al. [25] demonstrated the necessity of consideration of evaporation during the process. Khairallah and Anderson [26] presented a single-track thermo-fluid model to simulate the L-PBF process of stainless steel proposing the optimum process parameters to avoid residual pores. Shrestha and Chou [27] and Bayat et al. [28] developed 3D thermo-fluid models to investigate the pore formation in the L-PBF process and compare the conduction and keyhole mode behavior of melt pool resulting from using different process parameters. By including the recoil pressure and laser ray tracing energy source in their single-track simulation, Khairallah et al. [29] categorized the pore defects into three types of depression collapse, lateral pores, and trapped pores, and discussed the strategies to avoid them. They also illustrated the physical mechanisms behind sparking, spattering, and denudation in the PBF process by identifying three distinct zones along a melt track, i.e., depression, transition, and tail end.

Despite the advancements in the PBF modeling and simulation approaches, most of the developed models are limited to a single scan track or a single layer, while many of the internal pores are formed due to the layer-wise nature of this process, and many microstructural features are developed during the process of adding subsequent layers. Some multi-layer models are developed in the literature. Khan et al. [30] proposed a conduction-based model with an adaptive remeshing framework for quick assessment of the L-PBF process variables on the melt pool size. Cummins et al. [31] developed a coupled DEM/smoothed particle hydrodynamics (SPH) to simulate the evolving temperature and microstructure of non-spherical Ti6Al4V powder particles during the L-PBF process. Shi et al. [32] developed a finite element model of two layers focusing on the effects of processing conditions on the thermal behavior of the first layer during the melting of the second layer. Ricci et al. [33] presented a 3D FE model for the prediction of the temperature field during the L-PBF of AlSi10Mg alloy in five layers. The model was validated with experimental melt pool size and correlated to the microstructural properties at different layers. Afrasiabi et al. [34] presented a 2D numerical framework based on the SPH method with the successive building of ten layers using two different laser powers to show how the unevenness of layers can be avoided by adjusting the laser power during the L-PBF process. He et al. [35] presented a thermo-fluid model of double-layer SLM and studied the effects of laser power and hatch spacing on the remolten region between two scan tracks and two layers. Bayat et al. [36] developed a multi-physics of three-layer PBF to analyze the formation and evolution of lack-of-fusion pores and found more defects in the lower layers due to the lower temperature of the build platform. Koepf et al. [37] introduced a 3D crystal growth model to obtain the grain structures in the PBF of Inconel 718. Gan et al. [38] presented a multi-physics model of six-layer PBF to calculate melt pool dimensions and microstructure of Ni-based alloy parts. Using a 3D finite element model, Machirori et al. [39] examined the influences of various scanning strategies on the distribution of residual stresses during the multi-layer L-PBF of Ti6Al4V. Wu et al. [40] developed a numerical model to understand the consolidation mechanism in a multi-layer process of electron beam PBF.

There are also some other works on multi-layer modeling of the PBF process [41–44], however, most of them do not include the non-uniformity of the powder particle sizes and instead a uniform size distribution or a continuum media with different material properties was considered as the powder layer. Also, the laser-material interaction model is only based on a moving volumetric heat source, without considering the recoil pressure and Marangoni convection, which according to [29], results in unrealistic melting, flowing, and solidification of the material. So, the objective of the present study is to demonstrate the feasibility of multi-layer modeling of the L-PBF process without the above-mentioned limitations and to discuss the potential and challenges of such models. The overall taken approach is to use the discrete element method (DEM) to simulate the distribution of layers of powder particles over a build platform/previously melted and solidified layers, then to use the results to simulate the laser-powder interactions in the L-PBF

Table 1
Ti6Al4V material properties used for the DEM simulation.

Property	Density (kg/m^3)	Modulus of elasticity (GPa)	Poisson's ratio	Coefficient of restitution	Sliding friction coefficient	Rolling friction coefficient
Value	4420	114	0.34	0.5	0.5	0.1

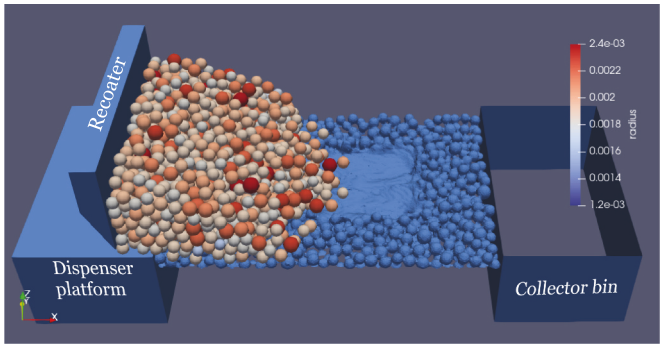

Fig. 2. Powder distribution of the 10th layer in Paraview. The legend indicates the particle size in cm.

Table 2
Ti6Al4V material properties used in the thermo-fluid model [53–55].

Properties	Values	Properties	Values
Solidus temperature, T_s (K)	1878	Liquidus temperature, T_L (K)	1928
Latent heat of fusion, L_f (kJ/kg)	286	Boiling temperature, T_v (K)	3533
Latent heat of evaporation (kJ/kg)	9830	Viscosity (kg/m s)	0.005
Surface tension gradient (N/m K)	−0.00026	Surface tension (N/m)	1.68

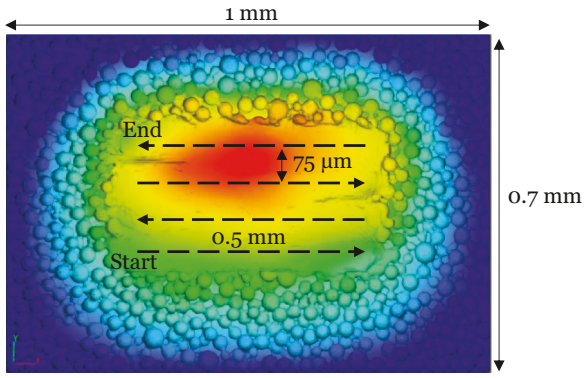

Fig. 3. A top view of the CFD results of the first layer showing the laser scan moving paths with dashed arrows and the domain size.

process using computational fluid dynamics (CFD). The combination of the DEM and CFD was developed and described in detail in our previous work [27]. Now by repeating this process, a thermo-fluid model of the multi-layer L-PBF process is developed in the present work that can be utilized as a foundation for understanding the basic physical phenomena and selecting the key process parameters. Such a model has the potential to be used as an effective tool for minimizing porosity defects in the fabricated parts by optimizing the process parameters and scanning strategies. It can also provide accurate temperature profiles to thermo-metallurgical and FEM-based models for predicting microstructure and residual stress evolution, respectively. Furthermore, the model's predictive capabilities can be applied to control strategies, such as the development of digital twins for metal additive manufacturing processes [45].

2. Methodologies

2.1. Multi-layer modeling procedure

The integrated multilayer L-PBF process simulation was implemented based upon two steps, i.e., powder deposition using the discrete element method (DEM) for each layer, followed by laser-powder interaction using computational fluid dynamics (CFD). The combination of DEM and CFD was developed for single-layer L-PBF in our previous research [27]. After the DEM simulation of each layer, the STL file, containing the distributed powder, was used for the CFD step, and the results from the CFD simulation were exported as an STL file. The top surface of the STL file, including the melted region and surrounding powders, obtained from the CFD simulation was cut out from the Stereolithography (STL) file to be used as the new substrate for the DEM simulation of the next layer. This was done to reduce the number of rectangles in the STL file thus reducing the DEM computational time. After the DEM simulation was performed, the new distributed powder layer was placed on the STL file obtained from the CFD of the previous layer, including the top surface geometry and pores formed during all the previously processed layers. The methodology cycle is illustrated in Fig. 1. This process was repeated until the desired number of layers was achieved.

2.2. Powder deposition modeling

The powder deposition was modeled using the open-source DEM code LIGGGHTS (LAMMPS Improved for General Granular and Granular Heat Transfer Simulations) [46]. In this model, contact forces (normal and tangential) and rolling friction are considered between particles. All particles in the computational domain are tracked by solving their trajectories and are identified separately by their size, mass, moment of inertia, etc. The force balance for a particle with index i is presented in the following equations [27]:

$$m_i\ddot{x}_i = F_{i,n} + F_{i,t} + F_{i,b} \quad (1)$$

$$I_i\frac{d\omega_i}{dt} = r_{i,c} \times F_{i,t} + T_{i,r} \quad (2)$$

where $F_{i,\,n}$ and $F_{i,\,t}$ are the normal and tangential particle-particle contact forces, respectively, and $F_{i,\,b}$ is the body force (gravity in this case). $r_{i,\,c} \times F_{i,\,t}$ represents the torque due to the tangential force. $T_{i,\,r}$ is an additional torque on the particle to account for non-sphericity through rolling friction. This term, however, is not considered since only spherical particles are taken into account in this model. More details about the particle-particle contact model can be found in Ref. [46]. The material properties used in this model are presented in Table 1. A time-step size of 50 ns and a particle size distribution of 16 µm to 48 µm were used for the DEM simulation. For the first layer, a 1-mm-long and 0.7-mm-wide flat surface was used as the build platform. After the DEM simulation is completed, Paraview version 5.9.1, which is an open-source multiple-platform software application, was used for visualizations. Fig. 2 shows the powder particle distribution of the 10th layer in Paraview.

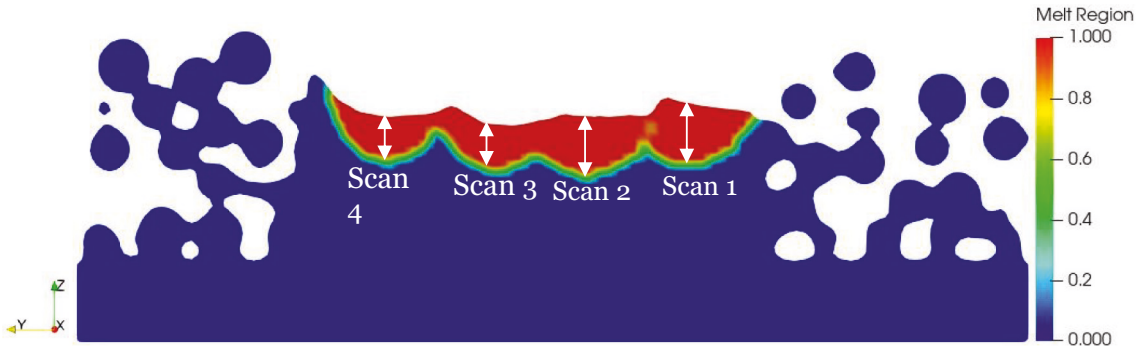

Fig. 4. Example of the total melt height measurement of four scan lines at layer 4 in Flow-3D Post.

Table 3
Simulation details for raster scanning (four 0.5-mm long laser scans) in an area of 1 mm in the x-direction and 0.7 mm in the y-direction in 10 layers.

Layer #	Simulation	Platform/computer	Number of processors	Number of triangles	Computational time (hours)	
Layer 1	DEM	Local workstation[a]	32	2	1.75	6.00
	Thermo-fluid	Local workstation[b]	36	–	4.25	
Layer 2	DEM	HPC[c]	48	270,165	110.75	116.25
	Thermo-fluid	Local workstation[b]	36	–	5.50	
Layer 3	DEM	HPC	60	326,470	138.75	147.00
	Thermo-fluid	Local workstation[b]	36	–	8.25	
Layer 4	DEM	HPC	60	374,792	191.50	200.25
	Thermo-fluid	Local workstation[b]	36	–	8.75	
Layer 5	DEM	HPC	60	272,628	126.00	137.50
	Thermo-fluid	Local workstation[b]	36	–	11.50	
Layer 6	DEM	HPC	60	255,581	142.25	149.25
	Thermo-fluid	Local workstation[b]	36	–	7.00	
Layer 7	DEM	HPC	60	342,915	114.25	123.75
	Thermo-fluid	Local workstation[b]	36	–	9.50	
Layer 8	DEM	HPC	60	301,313	97.00	106.75
	Thermo-fluid	Local workstation[b]	36	–	9.75	
Layer 9	DEM	HPC	60	320,716	136.75	146.75
	Thermo-fluid	Local workstation[b]	36	–	10.00	
Layer 10	DEM	HPC	60	303,459	102.75	113.75
	Thermo-fluid	Local workstation[b]	36	–	11.00	

[a] CPU: Intel Xeon E5-2687W0, 32, 3.10 GHz, RAM: 128 GB.
[b] CPU: Intel XeonE5-2695,36, 2.1/3.3 GHz, RAM: 512 GB.
[c] High-Performance Computing cluster at the University of Louisville (Cardinal Research Cluster).

2.3. Laser-powder interaction modeling

After the powder bed is obtained from the DEM simulation, it was saved as an STL file and imported to Flow-3D software version 11.2.6.4 (Flow Science, Inc., Santa Fe, New Mexico, USA). The computational domain in the CFD model consists of two immiscible phases, which are labeled as fluid (the metal region) and void (the ambient air). To determine the free surface of each phase, various methods have been proposed in the literature, including the level-set [47], the phase-field [48], and the volume-of-fluid (VOF) [49,50]. Flow-3D uses the VOF for tracking the phase interface, Fractional Area/Volume Obstacle Representation (FAVOR) method [51] for defining problem geometry, and CFD to solve thermo-fluid problems. For the present thermo-fluid model, an initial temperature of 308 K was considered for the entire computational domain. In addition, a thermal insulation boundary condition was applied on the four side walls and the bottom wall of the model. The main governing equations of mass, energy, and momentum conservation were solved during the CFD simulation:

Mass conservation:

$$\frac{\partial \rho}{\partial t} + \nabla.(\rho \vec{v}) = 0 \tag{3}$$

Momentum conservation:

$$\frac{\partial}{\partial t}(\rho \vec{v}) + \nabla.(\rho \vec{v}\vec{v}) = -\nabla p + \nabla.(\bar{\tau}) + \rho \vec{g} + S_{mom} \tag{4}$$

Energy conservation:

$$\frac{\partial(\rho H)}{\partial t} + \nabla.(\rho \vec{v} H) = \nabla.(k \nabla T) + S_h \tag{5}$$

where ρ is density, t is time, $\vec{v}$ is the fluid velocity, p is pressure, $\bar{\tau}$ is stress tensor, $\rho \vec{g}$ is gravitational body force, H is enthalpy, k is thermal conductivity, S_{mom} is momentum source, and S_h is the self-adaptive volumetric heat source. A moving Gaussian distribution heat source in the horizontal direction was considered for the laser beam. The flow is primarily governed by the surface tension which is defined by [27]:

$$\gamma = \gamma_m + \frac{d\gamma}{dT}\Delta T \tag{6}$$

where γ is the surface tension, γ_m is the surface tension at the melting point, $d\gamma/dT$ is the surface tension gradient, and ΔT is the temperature difference. During the simulation, the molten metal flow causes deformation in the surface, which is captured by the fluid fraction equation [27]:

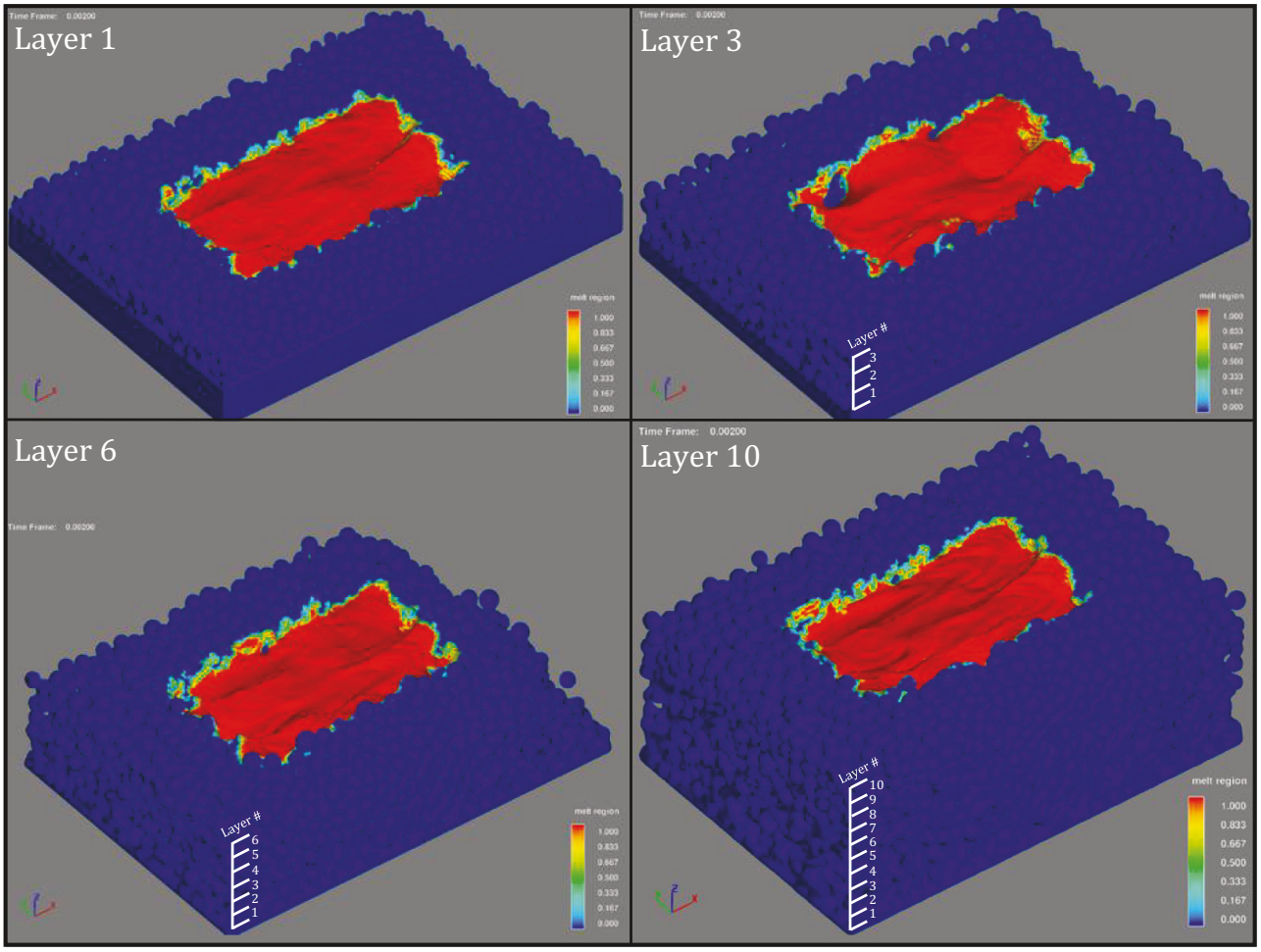

Fig. 5. Perspective views of the melt region of different layers of the multi-layer simulation.

Table 4
Surface roughness values obtained from the simulation of each layer.

Layer #	1	2	3	4	5	6	7	8	9	10
S_a (μm)	4.4	6.7	12.4	6.5	5.9	4.2	8.0	5.5	5.8	4.9

$$\frac{\partial F}{\partial t} + (V.\nabla)F = 0 \tag{7}$$

Also, as it is discussed in our previous research [27], recoil pressure caused by metal evaporation is modeled by the pressure boundary condition:

$$P_{recoil} = 0.54 P_0 exp\left(\frac{\Delta H_v (T - T_v)}{RTT_v}\right) \tag{8}$$

where P_0 is the atmospheric pressure, ΔH_v is the specific enthalpy of metal vapor, T_v is the boiling temperature, T is the surface temperature, and R is the universal gas constant. Additionally, multiple reflections of the laser between powder particles and within a possible keyhole are approximated by Fresnel reflection as [52]:

$$a = 1 - \frac{1}{2}\left(\frac{1 + (1 - \varepsilon cos\varnothing)^2}{1 + (1 + \varepsilon cos\varnothing)^2} + \frac{\varepsilon^2 - 2\varepsilon cos\varnothing + 2cos^2\varnothing}{\varepsilon^2 + 2\varepsilon cos\varnothing + 2cos^2\varnothing}\right) \tag{9}$$

where $\varnothing$ is the angle between the irradiated ray and the surface normal, ε depends on material properties and laser type and can be represented as:

$$\varepsilon^2 = \frac{2\varepsilon_2}{\varepsilon_1 + \left[\varepsilon_1^2 + \left(\frac{\sigma_{st}}{\omega\varepsilon_0}\right)^2\right]} \tag{10}$$

where ε_1 and ε_2 are the dielectric constants, ε_0 the permittivity of vacuum, σ_{st} is the electrical conductance per unit depth, and ω is the angular frequency of the laser. The Ti6Al4V powder's physical properties such as thermal conductivity, specific heat, and density were considered as functions of temperature. The constant properties of the Ti6Al4V powders used in the thermo-fluid simulation are presented in Table 2. It is worth mentioning that there are uncertainties in the material properties, which can affect the simulation results, e.g., melt pool geometry, surface morphology, etc., and can be the subject of a future study.

A hexahedral mesh of 5 μm is applied to the computational domain. The flow was assumed to be viscous, incompressible, and laminar and the fluid was Newtonian. Since Flow-3d [56] utilizes VOF and these models are typically used to capture the interface between only two phases, solid and liquid in this case, inert gas dynamics cannot be considered in this model; However, their effects are captured implicitly by applying the pressure effect and the cooling effect on the free surface of the material. This free surface can be between the material and either

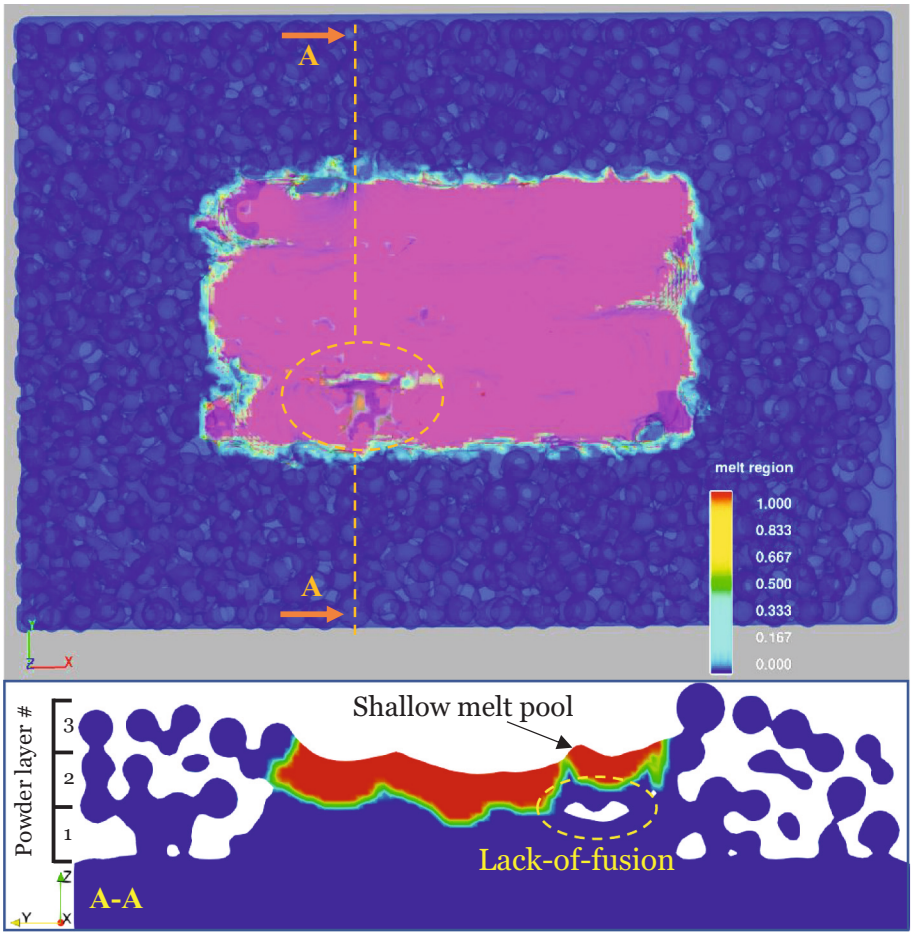

Fig. 6. An example of a lack-of-fusion defect during the simulation of layer three (top) transparent domain to show the defect location (bottom) A-A cross-section in the X-direction.

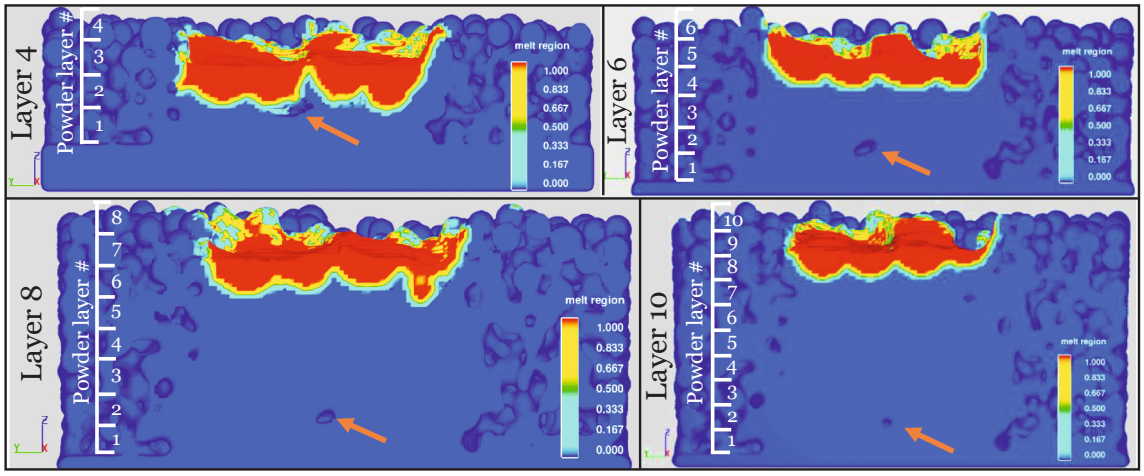

Fig. 7. The size decrement of a defect by increasing the number of layers. The cross-section is perpendicular to the scanning direction.

Table 5
The size of a pore measured after deposition and melting of different layers.

Layer #	4	5	6	7	8	9	10
Pore size (μm)	132.5	102.3	91.5	73.6	68.3	53.8	40.1

the surrounding volume or the pores inside the domain. Solid particles, including the solid powder particles of the current layer, as well as the ones of the previous layers, were assumed to be static and no spattering of material was considered for the model. Also, enough dwell time was assumed between each layer for the previous layer to cool down and reach the steady initial temperature. The melt pool geometry predictions were validated against experiments in previously published research by our group [27]. The parameters used for this process include laser power

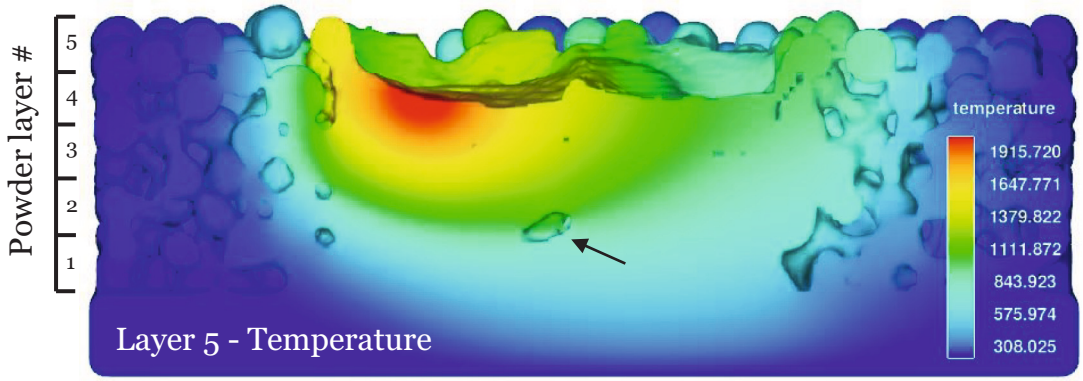

Fig. 8. Temperature distribution at the same cross-section as Fig. 6 shows a temperature range of ~1200 °C around the lack-of-fusion defect after scanning the fifth layer.

Table 6
Total melt height measurement results for different scans at different layers (each value is an average of five measurements along the scan length).

	Scan 1	Scan 2	Scan 3	Scan 4	Average
Layer 1	29.1 ± 1.0	34.0 ± 2.9	34.7 ± 2.2	33.7 ± 3.3	32.9 ± 1.3
Layer 2	30.9 ± 3.7	39.0 ± 2.9	32.7 ± 2.8	39.7 ± 1.8	35.6 ± 1.6
Layer 3	36.1 ± 4.2	39.6 ± 2.5	38.3 ± 3.5	37.9 ± 4.3	38.0 ± 1.7
Layer 4	39.2 ± 5.4	44.2 ± 1.2	40.4 ± 1.6	39.3 ± 3.9	40.3 ± 1.6
Layer 5	35.2 ± 5.0	38.2 ± 2.5	40.8 ± 2.3	39.6 ± 4.2	38.5 ± 1.8
Layer 6	36.0 ± 1.4	37.7 ± 1.8	39.3 ± 1.8	41.0 ± 2.4	38.5 ± 1.0
Layer 7	31.9 ± 1.4	35.9 ± 4.3	44.0 ± 4.8	42.6 ± 5.4	38.6 ± 2.2
Layer 8	40.6 ± 2.8	42.5 ± 3.1	42.1 ± 1.6	37.5 ± 3.2	40.7 ± 1.3
Layer 9	37.3 ± 4.4	41.8 ± 1.9	41.7 ± 4.3	45.1 ± 2.7	41.5 ± 1.7
Layer 10	40.9 ± 2.9	40.9 ± 2.4	43.6 ± 4.0	39.6 ± 3.4	41.3 ± 1.5
Average	35.7 ± 1.2	39.2 ± 0.9	39.8 ± 1.0	39.6 ± 1.3	

of 120 W, a scan speed of 1500 mm/s, and hatch spacing of 75 μm. Four parallel 0.5-mm-long laser scans were performed on each layer of powders. Fig. 3 shows the domain size of the first layer in Flow-3D, which was exported as an STL file and used as the new substrate for the DEM simulation of the next layer.

Melt pool measurements were performed in Flow-3D Post software version 11.2.6.4 (Flow Science, Inc., Santa Fe, New Mexico, USA). Since for layers two and higher, it is not possible to exactly distinguish the melt pool depth and the bead height in the melt region, the total melt height, which includes melt pool depth plus bead height, was measured to compare different scans/layers. Fig. 4 shows an example of the measured total height of the four scan tracks at layer four in Flow-3D Post. The measurements were done at five equally spaced cross-sections at 50 μm, 150 μm, 250 μm, 350 μm, and 450 μm along the scan length in each layer and the average value of the five measurements was reported for each scan at each layer.

3. Results and discussion

Table 3 shows the computational time and details of both DEM and CFD simulations for each layer. It can be seen that the simulation time is directly influenced by the number of triangles in the STL file. As by adding each layer, more powder particles, thus more geometrical features were added to the STL file for the next layer and therefore the simulation time was increased. This effect was minimized by cutting the unnecessary regions of the STL file to decrease the number of imported triangles to the DEM simulation. Mesh processing of STL files was performed in MeshLab software v. 2021.10 (ISTI - CNR). The typical melted region for some layers is shown in Fig. 5. The surface data of each layer was extracted and used to calculate the surface roughness presented in Table 4.

The surface roughness values range from 4 μm to 8 μm for all layers except for layer three, which is much higher. The high surface variations of layer three are visible in Fig. 5, as well. A possible reason is the formation of some lack-of-fusion defects in its previous layer causing disruptions in the melt pool at this layer. Generally, pore formation can be considered a random phenomenon in the L-PBF process, while the pore type and the likelihood of its formation can be estimated based on the process parameters [57,58]. Lack-of-fusion porosity may arise from incomplete melting of the powder due to insufficient thermal energy densities, particularly when melt pools are too small to form a complete overlap with the adjacent melt tracks or the previously melted layers

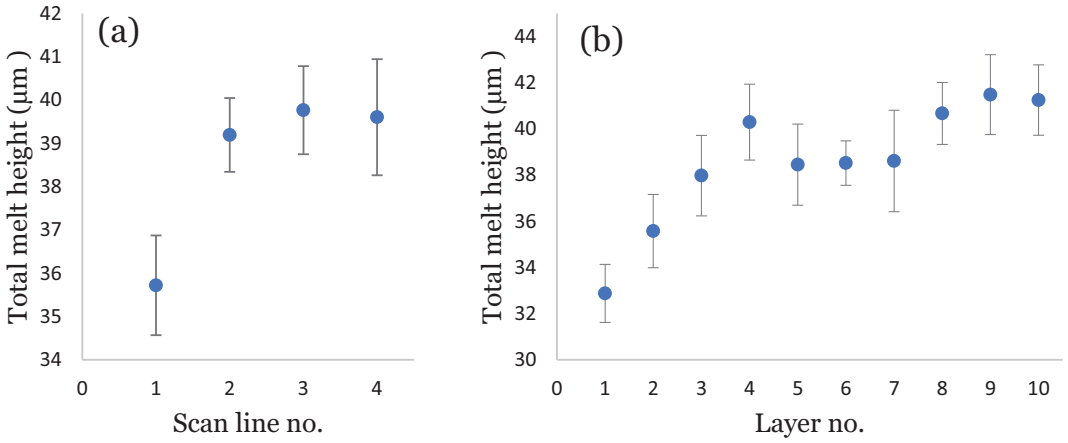

Fig. 9. The variations of average total melt height at (a) different scans and (b) different layers.

[59]. Insufficient thermal energy densities can be either due to low laser powers, high scan speeds, high distances between the scan lines, high layer thicknesses, or a combination of these cases. Since the process parameters used for this simulation, especially the high scanning speed, result in a lower volumetric energy density than what is recommended for part fabrication using Ti6Al4V [60], shallower melt pools were formed leading to insufficient overlap between the melt pool and the previously melted layer, which increases the likelihood of these pores being lack-of-fusion pores. Fig. 6 shows an example of a lack-of-fusion defect after the laser melting of the third layer.

The formation of these inter-layer pores can be a combined effect of a lack-of-sufficient heat to make the melt pool deep enough to penetrate the previous layers and high variations in the surface height of the previous layers (layer three's high surface roughness, in this case). So, to minimize the formation of these pores, higher laser power and/or lower scanning speed may be used. It was observed that the size of the pores decreases as more layers are deposited on the top and the number of layers increases. This can be attributed to receiving additional thermal energy resulting from scanning the next layers, which is in line with the results observed in the literature in simulation [36] as well as experiments [6,61]. Fig. 7 illustrates tracking an inter-layer lack-of-fusion defect, which was formed between layer three and layer four, through different layers. The size of this pore at its elongation direction at different stages of the simulation is listed in Table 5. Also, Fig. 8 shows the temperature distribution at the same cross-section as Fig. 7, indicating a temperature range of ~1200 °C around the lack-of-fusion defect after scanning the next subsequent layer (layer five).

The results of the total melt height are presented in Table 6. Each value is an average of five measurements along the length of a scan track. Fig. 9 illustrates the variations of average total melt height at different scans and different layers. Fig. 9 (a) shows the total melt height increases drastically and plateaus out from the first to the second scan. This behavior can be attributed to the lower average temperature of the part during the first scan, as opposed to it being pre-heated for the next scans causing heat accumulation and increment of total melt height. Also, Fig. 9 (b) shows an increase in the average value of the total melt height in the first four layers reaching a semi-steady state after layer four. This behavior is consistent with the observations in the literature [62] and can be attributed to the increment of the conduction path by increasing the number of layers, as conduction is the main phenomenon controlling the melt pool size.

4. Conclusions

To demonstrate the feasibility of multi-layer simulations in building small features by L-PBF, a 3D thermo-fluid model has been developed to simulate the multi-layer L-PBF process using DEM and CFD to simulate the particle distribution in the powder bed, and the laser-powder interaction, respectively. A moving Gaussian heat source, surface tension gradient, and evaporation pressure along with multiple reflections were included to predict the temperature distribution and history as well as melt pools and the top surface morphology from each layer. The model includes a surface tracking algorithm to account for the geometry of voids and lack-of-fusion pores generated during the process. Pore tracking during the multi-layer simulation shows the evolution of pores: forming, shrinking, or disappearing due to the interaction with the molten pool during scanning in subsequent layers. Also, the result implies that pore formation during laser PBF processing could be possibly attributed to a very rough surface from the previous layer. The findings suggest that the lack-of-fusion defects (1) elongate perpendicular to the build direction between layers and (2) may close possibly due to receiving more thermal energy from the laser during the scanning of the subsequent layers. One major limitation of the developed method is that the powder particles are assumed to be static during laser-powder interactions, thus no spattering or powder particle attraction to the melt pool can be observed. To extend this method to a larger-scale model, e.g., a higher number of layers with a larger scan area and different SLM process parameters (e.g., lower scan speeds), there will be a need to advance the computational power in terms of hardware processing capabilities and memories in order to avoid the high computational time especially associated with the DEM simulation of a larger area. In future work, the feasibility of using this method to investigate the local morphology at up-skin and down-skin surfaces of inclined parts will be explored. Also, in the continued work, small-scaled laser PBF experiments will be conducted for comparison and to address the weakness in model validations, before the model can be extended to further studies.

Declaration of competing interest

The authors declare that they have no known competing financial interests or personal relationships that could have appeared to influence the work reported in this paper.

Acknowledgments

This research was supported by the National Science Foundation (NSF) under Grant Number # 1921263.

References

[1] Fotovvati B, Etesami SA, Asadi E. Process-property-geometry correlations for additively-manufactured Ti–6Al–4V sheets. Mater Sci Eng A 2019;760:431–47. https://doi.org/10.1016/J.MSEA.2019.06.020.
[2] Cai C, Tey WS, Chen J, Zhu W, Liu X, Liu T, et al. Comparative study on 3D printing of polyamide 12 by selective laser sintering and multi jet fusion. J Mater Process Technol 2021;288:116882. https://doi.org/10.1016/J.JMATPROTEC.2020.116882.
[3] Zhang LC, Liu Y, Li S, Hao Y. Additive manufacturing of titanium alloys by electron beam melting: a review. Adv Eng Mater 2018;20:1700842. https://doi.org/10.1002/ADEM.201700842.
[4] Mehrpouya M, Dehghanghadikolaei A, Fotovvati B, Vosooghnia A, Emamian SS, Gisario A. The potential of additive manufacturing in the smart factory industrial 4.0: a review. Applied Sciences 2019;9:3865. https://doi.org/10.3390/APP9183865.
[5] Schwerz C, Raza A, Lei X, Nyborg L, Hryha E, Wirdelius H. In-situ detection of redeposited spatter and its influence on the formation of internal flaws in laser powder bed fusion. Addit Manuf 2021;47:102370. https://doi.org/10.1016/J.ADDMA.2021.102370.
[6] Bruna-Rosso C, Demir AG, Previtali B. Selective laser melting finite element modeling: validation with high-speed imaging and lack of fusion defects prediction. Mater Design 2018;156:143–53. https://doi.org/10.1016/J.MATDES.2018.06.037.
[7] Foroozmehr A, Badrossamay M, Foroozmehr E, Golabi S. Finite element simulation of selective laser melting process considering optical penetration depth of laser in powder bed. Mater Design 2016;89:255–63. https://doi.org/10.1016/J.MATDES.2015.10.002.
[8] Criales LE, Arısoy YM, Özel T. Sensitivity analysis of material and process parameters in finite element modeling of selective laser melting of inconel 625. Int J Adv Manuf Technol 2016;86(9):2653–66. https://doi.org/10.1007/S00170-015-8329-Y.
[9] Huang Y, Yang LJ, Du XZ, Yang YP. Finite element analysis of thermal behavior of metal powder during selective laser melting. Int J Therm Sci 2016;104:146–57. https://doi.org/10.1016/J.IJTHERMALSCI.2016.01.007.
[10] Antony K, Arivazhagan N, Senthilkumaran K. Numerical and experimental investigations on laser melting of stainless steel 316L metal powders. J Manuf Process 2014;16:345–55. https://doi.org/10.1016/J.JMAPRO.2014.04.001.
[11] Loh LE, Chua CK, Yeong WY, Song J, Mapar M, Sing SL, et al. Numerical investigation and an effective modelling on the selective laser melting (SLM) process with aluminium alloy 6061. Int J Heat Mass Transfer 2015;80:288–300. https://doi.org/10.1016/J.IJHEATMASSTRANSFER.2014.09.014.
[12] Mohanty S, Hattel J. Cellular scanning strategy for selective laser melting: capturing thermal trends with a low-fidelity, pseudo-analytical model. Math Probl Eng 2014;2014. https://doi.org/10.1155/2014/715058.
[13] Lee YS, Zhang W. Modeling of heat transfer, fluid flow and solidification microstructure of nickel-base superalloy fabricated by laser powder bed fusion. Addit Manuf 2016;12:178–88. https://doi.org/10.1016/J.ADDMA.2016.05.003.
[14] de Baere D, Bayat M, Mohanty S, Hattel J. Thermo-fluid-metallurgical modelling of the selective laser melting process chain. Procedia CIRP 2018;74:87–91. https://doi.org/10.1016/J.PROCIR.2018.08.035.
[15] Parry L, Ashcroft IA, Wildman RD. Understanding the effect of laser scan strategy on residual stress in selective laser melting through thermo-mechanical simulation. Addit Manuf 2016;12:1–15. https://doi.org/10.1016/J.ADDMA.2016.05.014.
[16] Gouge M, Denlinger E, Irwin J, Li C, Michaleris P. Experimental validation of thermo-mechanical part-scale modeling for laser powder bed fusion processes. Addit Manuf 2019;29:100771. https://doi.org/10.1016/J.ADDMA.2019.06.022.

[17] Nagesha BK, Anand Kumar S, Vinodh K, Pathania A, Barad S. A thermo – mechanical modelling approach on the residual stress prediction of SLM processed HPNGV aeroengine part. Mater Today: Proc 2021;44:4990–6. https://doi.org/10.1016/J.MATPR.2020.12.940.
[18] Yu T, Li M, Breaux A, Atri M, Obeidat S, Ma C. Experimental and numerical study on residual stress and geometric distortion in powder bed fusion process. J Manuf Process 2019;46:214–24. https://doi.org/10.1016/J.JMAPRO.2019.09.010.
[19] Panda BK, Sahoo S. Thermo-mechanical modeling and validation of stress field during laser powder bed fusion of AlSi10Mg built part. Results Phys 2019;12:1372–81. https://doi.org/10.1016/J.RINP.2019.01.002.
[20] Peng H, Ghasri-Khouzani M, Gong S, Attardo R, Ostiguy P, Rogge RB, et al. Fast prediction of thermal distortion in metal powder bed fusion additive manufacturing: part 2, a quasi-static thermo-mechanical model. Addit Manuf 2018;22:869–82. https://doi.org/10.1016/J.ADDMA.2018.05.001.
[21] Bayat M, Klingaa CG, Mohanty S, de Baere D, Thorborg J, Tiedje NS, et al. Part-scale thermo-mechanical modelling of distortions in laser powder bed fusion – analysis of the sequential flash heating method with experimental validation. Addit Manuf 2020;36:101508. https://doi.org/10.1016/J.ADDMA.2020.101508.
[22] Carraturo M, Jomo J, Kollmannsberger S, Reali A, Auricchio F, Rank E. Modeling and experimental validation of an immersed thermo-mechanical part-scale analysis for laser powder bed fusion processes. Addit Manuf 2020;36:101498. https://doi.org/10.1016/J.ADDMA.2020.101498.
[23] de Baere D, van Cauwenbergh P, Bayat M, Mohanty S, Thorborg J, Thijs L, et al. Thermo-mechanical modelling of stress relief heat treatments after laser-based powder bed fusion. Addit Manuf 2021;38:101818. https://doi.org/10.1016/J.ADDMA.2020.101818.
[24] Bayat M, Dong W, Thorborg J, To AC, Hattel JH. A review of multi-scale and multi-physics simulations of metal additive manufacturing processes with focus on modeling strategies. Addit Manuf 2021;47:102278. https://doi.org/10.1016/J.ADDMA.2021.102278.
[25] Wu YC, San CH, Chang CH, Lin HJ, Marwan R, Baba S, et al. Numerical modeling of melt-pool behavior in selective laser melting with random powder distribution and experimental validation. J Mater Process Technol 2018;254:72–8. https://doi.org/10.1016/J.JMATPROTEC.2017.11.032.
[26] Khairallah SA, Anderson A. Mesoscopic simulation model of selective laser melting of stainless steel powder. J Mater Process Technol 2014;214:2627–36. https://doi.org/10.1016/J.JMATPROTEC.2014.06.001.
[27] Shrestha S, Kevin Chou Y. A numerical study on the keyhole formation during laser powder bed fusion process. Journal of Manufacturing Science and Engineering 2019;141. https://doi.org/10.1115/1.4044100.
[28] Bayat M, Thanki A, Mohanty S, Witvrouw A, Yang S, Thorborg J, et al. Keyhole-induced porosities in laser-based powder bed fusion (L-PBF) of Ti6Al4V: high-fidelity modelling and experimental validation. Addit Manuf 2019;30:100835. https://doi.org/10.1016/J.ADDMA.2019.100835.
[29] Khairallah SA, Anderson AT, Rubenchik A, King WE. Laser powder-bed fusion additive manufacturing: physics of complex melt flow and formation mechanisms of pores, spatter, and denudation zones. Acta Mater 2016;108:36–45. https://doi.org/10.1016/J.ACTAMAT.2016.02.014.
[30] Khan K, Mohr G, Hilgenberg K, De A. Probing a novel heat source model and adaptive remeshing technique to simulate laser powder bed fusion with experimental validation. Comput Mater Sci 2020;181:109752. https://doi.org/10.1016/J.COMMATSCI.2020.109752.
[31] Cummins S, Cleary PW, Delaney G, Phua A, Sinnott M, Gunasegaram D, et al. A coupled DEM/SPH computational model to simulate microstructure evolution in Ti-6Al-4V laser powder bed fusion processes. Metals 2021;11:858. https://doi.org/10.3390/MET11060858.
[32] Shi Q, Gu D, Xia M, Cao S, Rong T. Effects of laser processing parameters on thermal behavior and melting/solidification mechanism during selective laser melting of TiC/Inconel 718 composites. Optics Laser Technol 2016;84:9–22. https://doi.org/10.1016/J.OPTLASTEC.2016.04.009.
[33] Ricci S, Testa G, Iannitti G, Ruggiero A. Laser powder bed fusion of AlSi10Mg alloy: numerical investigation on the temperature field evolution. Forces Mech 2022;8:100109. https://doi.org/10.1016/J.FINMEC.2022.100109.
[34] Afrasiabi M, Lüthi C, Bambach M, Wegener K. Smoothed particle hydrodynamics modeling of the multi-layer laser powder bed fusion process. Procedia CIRP 2022;107:276–82. https://doi.org/10.1016/J.PROCIR.2022.04.045.
[35] He Q, Xia H, Liu J, Ao X, Lin S. Modeling and numerical studies of selective laser melting: multiphase flow, solidification and heat transfer. Mater Design 2020;196:109115. https://doi.org/10.1016/J.MATDES.2020.109115.
[36] Bayat M, Mohanty S, Hattel JH. Multiphysics modelling of lack-of-fusion voids formation and evolution in IN718 made by multi-track/multi-layer L-PBF. Int J Heat Mass Transfer 2019;139:95–114. https://doi.org/10.1016/J.IJHEATMASSTRANSFER.2019.05.003.
[37] Koepf JA, Gotterbarm MR, Markl M, Körner C. 3D multi-layer grain structure simulation of powder bed fusion additive manufacturing. Acta Mater 2018;152:119–26. https://doi.org/10.1016/J.ACTAMAT.2018.04.030.
[38] Gan Z, Liu H, Li S, He X, Yu G. Modeling of thermal behavior and mass transport in multi-layer laser additive manufacturing of Ni-based alloy on cast iron. Int J Heat Mass Transfer 2017;111:709–22. https://doi.org/10.1016/J.IJHEATMASSTRANSFER.2017.04.055.
[39] Machirori T, Liu FQ, Yin QY, Wei HL. Spatiotemporal variations of residual stresses during multi-track and multi-layer deposition for laser powder bed fusion of ti-6Al-4V. Comput Mater Sci 2021;195:110462. https://doi.org/10.1016/J.COMMATSCI.2021.110462.
[40] Wu C, Zafar MQ, Zhao H. Numerical investigation of consolidation mechanism in powder bed fusion considering layer characteristics during multilayer process. Int J Adv Manuf Technol 2021;113:2087–100. https://doi.org/10.1007/S00170-021-06768-2/FIGURES/15.
[41] Masoomi M, Thompson SM, Shamsaei N. Laser powder bed fusion of ti-6Al-4V parts: thermal modeling and mechanical implications. Int J Mach Tool Manuf 2017;118–119:73–90. https://doi.org/10.1016/J.IJMACHTOOLS.2017.04.007.
[42] Denlinger ER, Gouge M, Irwin J, Michaleris P. Thermomechanical model development and in situ experimental validation of the laser powder-bed fusion process. Addit Manuf 2017;16:73–80. https://doi.org/10.1016/J.ADDMA.2017.05.001.
[43] Yang YP, Jamshidinia M, Boulware P, Kelly SM. Prediction of microstructure, residual stress, and deformation in laser powder bed fusion process. Comput Mech 2018;61:599–615. https://doi.org/10.1007/S00466-017-1528-7/FIGURES/20.
[44] Han Q, Low KWQ, Gu Y, Wang X, Wang L, Song B, et al. The dynamics of reinforced particle migration in laser powder bed fusion of Ni-based composite. Powder Technol 2021;394:714–23. https://doi.org/10.1016/J.POWTEC.2021.09.005.
[45] Gunasegaram DR, Murphy AB, Barnard A, DebRoy T, Matthews MJ, Ladani L, et al. Towards developing multiscale-multiphysics models and their surrogates for digital twins of metal additive manufacturing. Addit Manuf 2021;46:102089. https://doi.org/10.1016/J.ADDMA.2021.102089.
[46] Kloss C, Goniva C, Hager A, Amberger S, Pirker S. Models, algorithms and validation for opensource DEM and CFD-DEM. Prog Comput Fluid Dyn 2012;12:140–52. https://doi.org/10.1504/PCFD.2012.047457.
[47] Sharma A. Level set method for computational multi-fluid dynamics: a review on developments, applications and analysis. Sadhana 2015;40:627–52. https://doi.org/10.1007/S12046-014-0329-3/FIGURES/5.
[48] Badalassi VE, Ceniceros HD, Banerjee S. Computation of multiphase systems with phase field models. J Comput Phys 2003;190:371–97. https://doi.org/10.1016/S0021-9991(03)00280-8.
[49] Gopala VR, van Wachem BGM. Volume of fluid methods for immiscible-fluid and free-surface flows. Chem Eng J 2008;141:204–21. https://doi.org/10.1016/J.CEJ.2007.12.035.
[50] Weymouth GD, Yue DKP. Conservative volume-of-fluid method for free-surface simulations on Cartesian-grids. J Comput Phys 2010;229:2853–65. https://doi.org/10.1016/J.JCP.2009.12.018.
[51] Hirt C, Hydrodynamics JS-C on NS, 4th undefined, 1985 undefined. A porosity technique for the definition of obstacles in rectangular cell meshes. TridTrbOrg n.d.
[52] Cho JH, Na SJ. Implementation of real-time multiple reflection and fresnel absorption of laser beam in keyhole. J Phys D Appl Phys 2006;39:5372. https://doi.org/10.1088/0022-3727/39/24/039.
[53] Welsch G, Boyer R, Collings EW. In: Materials Properties Handbook: Titanium Alloys. 2nd ed.xxii. Materials Park, OH: ASM International; 1998. p. 1176.
[54] Elmer JW, Palmer TA, Babu SS, Zhang W, DebRoy T. Phase transformation dynamics during welding of Ti–6Al–4V. J Appl Phys 2004;95:8327. https://doi.org/10.1063/1.1737476.
[55] Shrestha S, Chou K. A build surface study of powder-bed electron beam additive manufacturing by 3D thermo-fluid simulation and white-light interferometry. Int J Mach Tool Manuf 2017;121:37–49. https://doi.org/10.1016/J.IJMACHTOOLS.2017.04.005.
[56] Flow Science Inc. Santa Fe, NM, USA. FLOW-3D® Version 12.0 User's Manual (2018) [Online]. https://www.flow3d.com; 2018 (accessed July 31, 2022).
[57] Huang Y, Fleming TG, Clark SJ, Marussi S, Fezzaa K, Thiyagalingam J, et al. Keyhole fluctuation and pore formation mechanisms during laser powder bed fusion additive manufacturing. Nature Communications 2022;13:1–11. https://doi.org/10.1038/s41467-022-28694-x.
[58] Sanaei N, Fatemi A. Defects in additive manufactured metals and their effect on fatigue performance: a state-of-the-art review. Prog Mater Sci 2021;117:100724. https://doi.org/10.1016/J.PMATSCI.2020.100724.
[59] Promoppatum P, Srinivasan R, Quek SS, Msolli S, Shukla S, Johan NS, et al. Quantification and prediction of lack-of-fusion porosity in the high porosity regime during laser powder bed fusion of ti-6Al-4V. J Mater Process Technol 2022;300:117426. https://doi.org/10.1016/J.JMATPROTEC.2021.117426.
[60] Fotovvati B, Balasubramanian M, Asadi E. Modeling and optimization approaches of laser-based powder-bed fusion process for Ti-6Al-4V Alloy. Coatings 2020;10:1104. https://doi.org/10.3390/COATINGS10111104.
[61] Kurzynowski T, Stopyra W, Gruber K, Ziólkowski G, Kuznicka B, Chlebus E. Effect of scanning and support strategies on relative density of SLM-ed H13 steel in relation to specimen size. Materials 2019;12:239. https://doi.org/10.3390/MA12020239.
[62] Waqar S, Sun Q, Liu J, Guo K, Sun J. Numerical investigation of thermal behavior and melt pool morphology in multi-track multi-layer selective laser melting of the 316L steel. Int J Adv Manuf Technol 2021;112:879–95. https://doi.org/10.1007/S00170-020-06360-0/FIGURES/15.